SIAM J. IMAGING SCIENCES
Vol. 5, No. 1, pp. 465–482

One Shot Inverse Scattering via Rational Approximation*

Martin Hanke†

Abstract. We consider the two-dimensional inverse obstacle problem for the Helmholtz equation and aim for localizing several scatterers from the far field of the scattered wave for one fixed incident field and fixed frequency. Our method is independent of the physical properties of the scatterers and is based on a careful investigation of the decay of the tail of the Fourier coefficients of the given far field. Using Prony's method or, equivalently, certain rational Padé approximants, we determine a discrete set of point sources that produces a far field with approximately the same tail of Fourier coefficients. We further show how a repetition of this procedure for different virtual points of origin can be turned into a means for imaging the scatterers. Although this method suffers from a certain lack of stability in the presence of noise, it may provide a useful alternative imaging technique when the scatterers are small inhomogeneities and the number of measurements is as limited as described above.

Key words. inverse scattering, Helmholtz equation, Prony's method, MUSIC

AMS subject classifications. 35R30, 65N21

DOI. 10.1137/110823985

1. Introduction.

We treat a two-dimensional formulation of an inverse obstacle scattering problem for time-harmonic acoustic waves. Our goal is to recover information about the shape or the relevant features of the unknown scattering obstacles (there may be more than one) from the far field pattern of the scattered wave for one single incident field with fixed frequency. At the same time we want to stipulate as few assumptions as possible about the physical nature of the scatterers.

This problem has a long tradition, although the question is still open whether the given information is sufficient to determine the scatterers—even when their physical properties are known. Only for certain special cases are there known (positive) answers: Colton and Sleeman [10] (see also [9, Corollary 5.3]), for example, have shown that these data uniquely determine a sound-soft scatterer within a ball of the size of one wavelength. Uniqueness has also been settled for sound-soft (resp., sound-hard) *polygonal* scatterers by Alessandrini and Rondi [1], and Elschner and Yamamoto [13], without any constraint on their size.

There also exists a variety of numerical methods to reconstruct, or approximate, the scatterers from the given far field. If the physical nature of a single scatterer is known, standard Newton-type methods for more or less elaborate formulations of the problem (cf., e.g., Kress and Rundell [27] or Johansson and Sleeman [24]) are applicable; alternatively, there are the methods of Imbriale and Mittra [23], and of Kirsch and Kress (cf. [26]), that analytically continue the scattered field and then determine the boundary of the scatterer

*Received by the editors February 9, 2011; accepted for publication (in revised form) January 20, 2012; published electronically March 29, 2012.
http://www.siam.org/journals/siims/5-1/82398.html
†Institut für Mathematik, Johannes Gutenberg-Universität Mainz, 55099 Mainz, Germany (hanke@math.uni-mainz.de).

as those points where the field satisfies the respective boundary condition. Also the point source method by Potthast [33] should be mentioned here, as it employs a somewhat related approach.

Other methods aim for approximating the convex hull of the scatterers: Ikehata [22] has shown how to reconstruct (exactly) the convex hull of polygonal sound-soft scatterers, whereas the so-called convex scattering support introduced by Kusiak and Sylvester [29, 30] is independent of the geometry and physical properties of the scatterers but provides only a convex subset of their convex hull.

Finally, imaging functionals that backpropagate the given data have been considered in various works, e.g., in [3, 4, 15, 17, 34]. These imaging techniques can cope with one or several incoming waves and/or frequencies, but the resulting visualizations lack resolution if only one incoming wave is used.

In this paper we develop a new approach for imaging the scatterers, which utilizes ideas that are related to those in [22, 30]. In order to avoid a convexity assumption we approximate the scatterers via polar (or dipolar) sources, which we determine from the data. Similar ideas have a certain tradition in electrostatics (cf., e.g., [8, 12, 18, 19]), but apparently have not yet been applied to inverse scattering, despite the similarity of these two problems. We realize this approach very efficiently by using Prony's method to exploit the information content of medium size frequencies within the data, i.e., frequencies which constitute the superlinearly decaying tail of the Fourier transform of the far field. As we demonstrate, our method is capable of locating several small scatterers with arbitrary (unknown) physical properties. In this respect the output of the method is similar in spirit to the celebrated MUSIC algorithm (cf., e.g., [6, 11, 25, 36]), but in contrast to MUSIC we require only one column of the multistatic response matrix for the inversion. The method can also be used to visualize significant geometrical features of scatterers with finite extent, as we illustrate numerically, but this requires very accurate data. We mention that, alternatively, techniques from remote sensing can also be used to locate point scatterers, or so-called sparse objects; cf., e.g., Fannjiang, Strohmer, and Yan [14].

The outline of this paper is as follows. Once we have specified the problem setting in section 2, we go on in section 3 to develop a first algorithm to approximate polar sources from the Fourier transform of the far field, but this first version is not yet reliable enough to produce useful images of general scatterers. To obtain those we have to repeat the calculation for a sequence of fictitious points of origin; see section 4. In section 5 we illustrate the loss of performance of our method in the presence of noise. A certain improvement can be gained by using more than one incoming wave and the associated scattered far fields. A comparison with the MUSIC inversion (section 6) shows that our method is superior as long as the number of incoming waves is comparable to the number of the scatterers; otherwise the MUSIC scheme is more robust. We conclude in section 7 with a brief summary of our findings and with two straightforward extensions of our approach to slightly different settings. Finally, in the appendix we sketch the necessary modifications of our analysis for dipolar sources which are relevant for scatterers with general physical properties.

2. Problem setting.

Let

$$\Omega = \bigcup_{j=1}^{J} \Omega_j$$

be the union of a finite number of bounded and simply connected domains in $\mathbb{R}^2$ with C^2 boundary $\partial\Omega$. We assume that $\overline{\Omega}_i \cap \overline{\Omega}_j = \emptyset$ for $i \neq j$, and consider each $\overline{\Omega}_j$ to be the support of a scattering obstacle with unspecified physical properties, all of which are embedded in a homogeneous background. For later use we also introduce the radius

$$\rho \,=\, \max\big\{\, |z| : z \in \partial\Omega \,\big\} \tag{2.1}$$

of the smallest circle around the origin enclosing all of Ω.

Let u^i be a time-harmonic incident field with wave number $k > 0$, for example a point source, or a plane wave

$$u^i(x) \,=\, e^{\mathrm{i}kd\cdot x}\,, \qquad x \in \mathbb{R}^2\,, \tag{2.2}$$

with incident direction $d \in S^1$. Then the obstacles give rise to a time-harmonic scattered field u that satisfies the Helmholtz equation

$$\Delta u + k^2 u \,=\, 0 \qquad \text{in } \mathbb{R}^2 \setminus \overline{\Omega}\,, \tag{2.3}$$

together with the Sommerfeld radiation condition

$$\frac{\partial u}{\partial r} \,-\, \mathrm{i}ku \,=\, o(1/\sqrt{r}) \qquad \text{as } r = |x| \to \infty\,,$$

and with appropriate boundary/transmission conditions on $\partial\Omega$, reflecting the physical properties of the obstacle; for example, if Ω is a sound-soft obstacle, then

$$u \,=\, -u^i \qquad \text{on } \partial\Omega.$$

In any case it follows that u admits an asymptotic expansion near infinity of the form

$$u(r\widehat{x}) \,=\, \frac{e^{\mathrm{i}kr}}{\sqrt{r}}\, u^\infty(\widehat{x}) \,+\, O(r^{-3/2})\,, \qquad \widehat{x} \in S^1\,, \quad r \to \infty\,; \tag{2.4}$$

cf., e.g., Colton and Kress [9].

For ease of simplicity we assume in what follows that we can represent u as a single layer potential over $\partial\Omega$, i.e.,

$$u(x) \,=\, \int_{\partial\Omega} \Phi(x,z)\psi(z)\,\mathrm{d}s(z)\,, \qquad x \in \mathbb{R}^2 \setminus \overline{\Omega}\,, \tag{2.5}$$

with (complex) density ψ. Here,

$$\Phi(x,z) \,=\, \frac{\mathrm{i}}{4}\, H_0^{(1)}(k|x-z|)\,, \qquad x \in \mathbb{R}^2 \setminus \{z\}\,,$$

is the fundamental solution of the Helmholtz equation in $\mathbb{R}^2$, with $H_0^{(1)}$ the Hankel function of the first kind of order zero. Note that (2.5) is valid for sound-soft obstacles with $\psi = -\frac{\partial}{\partial\nu}(u + u^i)$ by Huygen's principle but may need some modifications for other scatterers; see

the appendix. For the moment this assumption allows us to extend the field u appropriately to all of $\mathbb{R}^2$ as the solution of a source problem

$$\Delta u + k^2 u \;=\; -F \qquad \text{in } \mathbb{R}^2\,, \tag{2.6}$$

where F is the distribution

$$F \;=\; \psi\, \mathrm{d}s(\partial\Omega) \tag{2.7}$$

supported on $\partial\Omega$; that is, if v is any C_0^∞ function in $\mathbb{R}^2$, then

$$\langle\, F, v\,\rangle \;=\; \int_{\partial\Omega} v(z)\psi(z)\,\mathrm{d}s\,.$$

Using the fact that

$$\Phi^\infty(\widehat{x}, z) \;=\; \frac{e^{\mathrm{i}\pi/4}}{\sqrt{8\pi k}}\, e^{-\mathrm{i}k\widehat{x}\cdot z}\,, \qquad \widehat{x}\in S^1\,, \quad z\in\mathbb{R}^2\,, \tag{2.8}$$

is the far field of $\Phi(\,\cdot\,, z)$, we conclude from (2.4) and (2.5) that the far field of u can be rewritten as

$$u^\infty(\widehat{x}) \;=\; \frac{e^{\mathrm{i}\pi/4}}{\sqrt{8\pi k}} \int_{\partial\Omega} e^{-\mathrm{i}k\widehat{x}\cdot z}\psi(z)\,\mathrm{d}s(z)\,.$$

For fixed $z\in\partial\Omega$ we now insert the Jacobi–Anger expansion (cf. [9])

$$e^{-\mathrm{i}k\widehat{x}\cdot z} \;=\; \sum_{n=-\infty}^{\infty} (-\mathrm{i})^n e^{-\mathrm{i}n\arg z} J_n(k|z|) e^{\mathrm{i}nt}\,, \tag{2.9}$$

where $\arg z$ is the polar angle φ of $z = |z|(\cos\varphi, \sin\varphi)$ and where $\widehat{x} = (\cos t, \sin t)$ with $0\le t, \varphi < 2\pi$. From this we obtain the Fourier series of the far field

$$u^\infty(\cos t, \sin t) \;=\; \sum_{n=-\infty}^{\infty} a_n e^{\mathrm{i}nt} \tag{2.10}$$

with

$$a_n \;=\; \frac{e^{\mathrm{i}\pi/4}}{\sqrt{8\pi k}}(-\mathrm{i})^n \int_{\partial\Omega} e^{-\mathrm{i}n\arg z} J_n(k|z|)\psi(z)\,\mathrm{d}s\,. \tag{2.11}$$

Figure 1 shows the absolute values $|a_n|$ over $n\in\mathbb{Z}$ for the Fourier coefficients of the far field of two sound-soft obstacles, each having a diameter of about one wavelength, and ρ of (2.1) being approximately $\rho\approx 10.4$; the wave number is $k=1$. The plot exhibits the typical behavior of these data, which roughly splits into three parts: The first one is the low-frequent spectrum, a zoom of which is shown in the right-hand plot. This part corresponds to frequencies associated with $|n| \lesssim k\rho$. Within this range, the Fourier coefficients are oscillating, in agreement with the corresponding behavior of the Bessel functions $J_n(k|\,\cdot\,|)$ that occur in

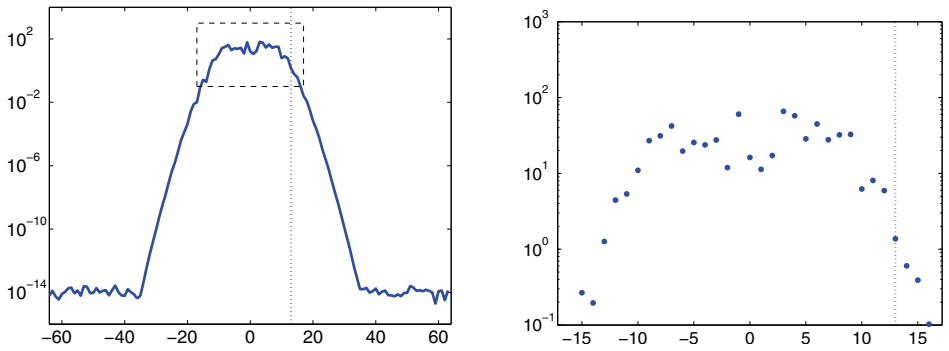

Figure 1. *Left: Fourier transform of the far field (absolute values). Right: Zoom in on the dashed area of the left-hand plot.*

(2.11). It is not clear at all how this part of the spectrum can be exploited efficiently to approach the inverse problem.

The second part of the spectrum, which we call its tail, starts with the medium sized frequencies corresponding to Fourier indices $|n| > k\rho$. The respective Fourier coefficients drop down to zero superlinearly, as the Bessel functions behave like

$$J_n(k\rho) \approx \begin{cases} \dfrac{1}{\Gamma(n+1)}\left(\dfrac{k\rho}{2}\right)^n, & n \gg k\rho\,, \\ \dfrac{(-1)^n}{\Gamma(|n|+1)}\left(\dfrac{k\rho}{2}\right)^{|n|}, & n \ll -k\rho\,; \end{cases} \tag{2.12}$$

cf., e.g., Gradshteyn and Ryzhik [16, 8.402]. A rough estimate of $k\rho$ can be obtained from a visual inspection of the Fourier spectrum. In our example we can use, e.g., the horizontal offset of the dotted vertical line in Figure 1 that separates these first two parts of the spectrum. This yields the estimate $k\rho \approx 13$ for this example.

It is this second part of the spectrum that we will utilize for our numerical reconstructions below, because it allows a very elegant extraction of relevant information about the scatterers at which we are aiming. Note, however, that in practice this region will be fairly small, as it is limited by the accuracy of the given data: In fact, the third part of the spectrum that we encounter in Figure 1 is the plateau of Fourier coefficients that starts here at about $|n| \approx 35$ and which consists of (numerical) noise only. For real data, the noise level will be larger, and the plateau will therefore be met much earlier; cf. section 5.

3. Pole fitting.

In this section we switch to complex variable notation by identifying the vector $z \in \mathbb{R}^2$ with the complex number $\zeta \in \mathbb{C}$. By abuse of notation, however, we will stick to writing Ω and ψ when we refer to the associated domain in $\mathbb{C}$ and the corresponding density from (2.5) evaluated at the boundary $\partial\Omega \subset \mathbb{C}$.

Taking into account that $\Omega \subset \{\zeta : |\zeta| \le \rho\}$ (cf. (2.1)), we can use this density ψ to define two functions

$$f_+(\widehat{\zeta}) = \int_{\partial\Omega} \frac{\overline{\psi(\eta)}}{\widehat{\zeta} - \eta/\rho}\, \mathrm{d}s(\eta) \tag{3.1}$$

and

$$f_-(\widehat{\zeta}) \;=\; \int_{\partial\Omega} \frac{\psi(\eta)}{\widehat{\zeta} - \eta/\rho}\, \mathrm{d}s(\eta)\,,$$

which are analytic in the exterior of Ω/ρ. Moreover, the two functions go to zero for $\widehat{\zeta} \to \infty$, and can be developed into Laurent series

$$f_+(\widehat{\zeta}) \;=\; \sum_{n=0}^{\infty} b_n \widehat{\zeta}^{-n-1}\,, \qquad f_-(\widehat{\zeta}) \;=\; \sum_{n=0}^{\infty} b_{-n} \widehat{\zeta}^{-n-1}\,, \tag{3.2}$$

which converge in the exterior of the unit disk.

Now assume that F of (2.7) (resp., $\overline{F}$) can be approximated as

$$\overline{F} \;=\; \overline{\psi}\, \mathrm{d}s(\partial\Omega) \;\approx\; \sum_{l=1}^{M} \lambda_l \delta_{\rho\widehat{\zeta}_l} \tag{3.3}$$

in the sense of distributions, where δ_η denotes the delta distribution located in $\eta \in \mathbb{C}$, $\widehat{\zeta}_l$, $l = 1, \ldots, M$, are certain points within the unit disk, and $\lambda_l \in \mathbb{C}$ are associated weights. Such an assumption is plausible if the scatterers are small in size, as has been shown in [5, 17, 20] for scatterers with various physical properties (penetrable, sound-soft, sound-hard, etc.). However, it may also hold when the scatterers are somewhat larger in size but have vertices that cause singularities of the scattered field. Inserting (3.3) in (3.1) it follows that

$$f_+(\widehat{\zeta}) \;\approx\; r_+(\widehat{\zeta}) \;=\; \sum_{l=1}^{M} \frac{\lambda_l}{\widehat{\zeta} - \widehat{\zeta}_l} \;=\; \sum_{n=0}^{\infty} \left(\sum_{l=1}^{M} \lambda_l \widehat{\zeta}_l^{\,n} \right) \widehat{\zeta}^{-n-1}\,, \tag{3.4}$$

which means that f_+ is close to a rational function r_+ with poles at $\widehat{\zeta}_l$, $l = 1, \ldots, M$. Furthermore, it follows from (3.2) that we have

$$b_n \;\approx\; \sum_{l=1}^{M} \lambda_l \widehat{\zeta}_l^{\,n}\,, \qquad n = 0, 1, 2, \ldots\,, \tag{3.5}$$

in this case. In (3.4) and (3.5), the approximate identities would turn into strict equalities if the model (3.3) were exact.

We now take the previous considerations as a motivation to adopt the approach taken in [19] for the Laplace equation to locate the individual obstacles by determining suitable rational approximations of $f_\pm$. It is our expectation to see the corresponding poles approximate the singularities of $f_\pm$ and thus to "cluster" near the scatterers Ω_j.

Starting from (2.11) and (2.12) we introduce

$$c_n \;=\; \Gamma(|n|+1) \left(\frac{2}{\mathrm{i}k\rho} \right)^{|n|} \frac{\sqrt{8\pi k}}{e^{-\mathrm{i}\pi/4}}\, \overline{a}_n\,, \qquad n \in \mathbb{Z}\,, \tag{3.6}$$

where ρ, again, is as in (2.1), such that

$$c_n \;\approx\; \int_{\partial\Omega} (\zeta/\rho)^n \overline{\psi(\zeta)}\, \mathrm{d}s \;=\; b_n\,, \qquad n \gg k\rho\,, \tag{3.7a}$$

and

$$\overline{c}_n \approx \int_{\partial\Omega} (\zeta/\rho)^{|n|}\psi(\zeta)\,\mathrm{d}s = b_n\,, \qquad n \ll -k\rho\,. \tag{3.7b}$$

Here, the approximate identities refer to the asymptotics (2.12) of the Bessel functions and are independent of the validity of (3.3). We conclude that the auxiliary coefficients c_n approximate the Laurent coefficients b_n of f_+ for $n \gg k\rho$, while their complex conjugates are close to the Laurent coefficients of f_- for $n \ll -k\rho$.

Note that we have access neither to f_+ explicitly nor to its full Laurent series. Still, by using Padé techniques, rational approximants of f_+ can be computed by using merely a finite window of the Laurent coefficients b_n: Rewriting r_+ of (3.4) as

$$r_+(\widehat{\zeta}) = \sum_{l=1}^{M} \frac{\lambda_l}{\widehat{\zeta} - \widehat{\zeta}_l} = \frac{q_{M-1}(\widehat{\zeta})}{p_M(\widehat{\zeta})}\,,$$

with two polynomials q_{M-1} and p_M of degrees $M-1$ and M, respectively, where

$$p_M(\widehat{\zeta}) = \widehat{\zeta}^M - \pi_{M-1}\widehat{\zeta}^{M-1} - \cdots - \pi_0 \tag{3.8}$$

with $\pi_l \in \mathbb{C}$, $l = 0, \ldots, M-1$, then we conclude from (3.2) and (3.4) that

$$\sum_{n=0}^{\infty} b_n \widehat{\zeta}^{-n-1} \approx \frac{q_{M-1}(\widehat{\zeta})}{p_M(\widehat{\zeta})}\,,$$

and hence, using (3.8),

$$\left(\sum_{n=0}^{\infty} b_n \widehat{\zeta}^{-n-1}\right)\left(\widehat{\zeta}^M - \sum_{l=0}^{M-1} \pi_l \widehat{\zeta}^l\right) \approx q_{M-1}(\widehat{\zeta})\,.$$

By comparing the expansion coefficients it follows that

$$b_{n+M} - \sum_{\nu=0}^{M-1} b_{n+\nu}\pi_\nu \approx 0\,, \qquad n = 0, 1, 2, \ldots. \tag{3.9}$$

Now, assume that for some $m, M \in \mathbb{N}$ the indices $n = m, \ldots, m+2M-1$ correspond to the aforementioned tail of the Fourier spectrum, where the Fourier coefficients a_n of the far field decay superlinearly, and hence $b_n \approx c_n$ by virtue of (3.7a). Then we can replace the corresponding b_n's by c_n's in (3.9), and turn the approximate identities into strict equalities to set up the linear system

$$\begin{bmatrix} c_m & c_{m+1} & c_{m+2} & \cdots & c_{m+M-1} \\ c_{m+1} & c_{m+2} & & & c_{m+M} \\ \vdots & & \ddots & & \vdots \\ c_{m+M-2} & & & c_{m+2M-4} & c_{m+2M-3} \\ c_{m+M-1} & & \cdots & c_{m+2M-3} & c_{m+2M-2} \end{bmatrix} \begin{bmatrix} \pi_0 \\ \pi_1 \\ \vdots \\ \pi_{M-2} \\ \pi_{M-1} \end{bmatrix} = \begin{bmatrix} c_{m+M} \\ c_{m+M-1} \\ \vdots \\ c_{m+2M-2} \\ c_{m+2M-1} \end{bmatrix}, \tag{3.10}$$

to be solved for approximate expansion coefficients π_l of the numerator polynomial p_M of r_+; cf. (3.8). The zeros $\widehat{\zeta}_l$ of the corresponding polynomial may then provide approximate source points for (3.3). Once these source points have been determined, one can treat the equations (3.5) with $n = m, \ldots, m + M - 1$, and c_n instead of b_n on the left-hand side, as a linear system for the corresponding residues λ_l, although these residues play a minor role only in our approach.

Note that it takes $2M$ Fourier coefficients to set up the linear system (3.10). Taking into account that we can use only those coefficients c_n with $n \gg k\rho$, we thus need at least $2(k\rho + 2M)$ reliable Fourier coefficients of the far field to determine M approximate locations of the obstacles Ω_j, $j = 1, \ldots, J$. In our experiments (see below), it has proved useful to choose M as large as possible—in particular, independent of any a priori information about the number J of scatterers—that is, we include in the inversion process as many of the Fourier coefficients of the far field as contribute to what we have called the second part of the Fourier spectrum.

The amount of work for computing the poles and residues from a given far field consists of (i) an FFT to determine the Fourier coefficients of the far field, (ii) the transformation of these Fourier coefficients to the coefficients c_n, (iii) the solution of the linear systems (3.10) and (3.5), and (iv) the determination of the roots of p_M of (3.8). If the far field is sampled at N equidistant points of S^1, the total work load is thus of the order $O(N \log N) + O(M^3)$, the second term being typically negligible.

We conclude this section with a couple of remarks and a first numerical exemplification of the suggested approach.

Remark 3.1. The particular implementation using (3.10) that we have sketched above is equivalent to what is known as Prony's method in the engineering literature; cf., e.g., [21, 36]. We refer the reader to Ammar, Dayawansa, and Martin [2] for the derivation of an alternative and more recommended numerical implementation of this method.

Remark 3.2. It has to be emphasized that there are no known theoretical results that establish that the poles of our rational approximations will be close to the scatterers Ω_j. There exist some very limited results about the locations of poles of Padé approximants of Stieltjes functions and few other function classes (cf., e.g., Baker and Graves-Morris [7]), but these do not apply to our particular setting. On the other hand, there is a counterexample by Lubinsky [32] which shows that the poles of Padé approximants can, in general, cluster anywhere in the complex plane as the degree of the approximants goes to infinity. Still, in applications (e.g., in circuit theory) it is standard numerical practice to use these poles to obtain some quantitative or qualitative understanding of the corresponding processes.

Remark 3.3. Finally, we emphasize that even in the degenerate case of J ideal point scatterers, i.e., when equality holds in (3.3), we cannot determine their locations exactly with our approach (whatever we choose for m and M), as the computable quantities c_n (resp., $\overline{c}_n$) approximate only the true Laurent coefficients $b_{\pm n}$ of $f_\pm$ (cf. (3.7)), and this approximation is merely of the order of $O(1/n)$. This further restricts the accuracy that can be achieved for this inverse problem.

Example 3.4. We illustrate our approach of localizing the scatterers for the particular example that has already served for Figure 1. Figure 2 shows the corresponding scatterers together with little spots for the resulting approximate source points (3.3) that are obtained

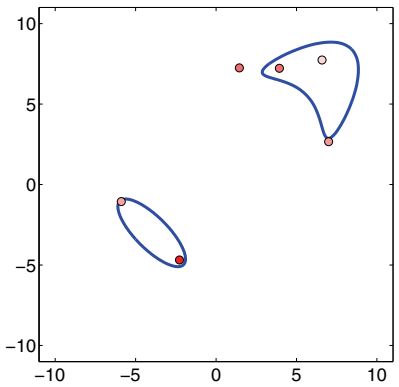

Figure 2. *True scatterers and their localizations.*

with this method. The intensity of the color of a spot encodes the magnitude of the associated residue λ_l: the darker the spot, the greater the residue. Only those (six) approximate source points are shown whose residues are above some (relative) threshold, i.e., that satisfy

$$|\lambda_l| \;\geq\; \varepsilon \max\{\, |\lambda_\nu| \,:\, \nu = 1, \ldots, M \,\} \qquad \text{with} \;\; \varepsilon = 10^{-2} \,.$$

It is nicely seen that the spots localize the distinct features of the extended scatterers.

For this "reconstruction" we have utilized the $2M = 22$ Fourier coefficients a_n of u^∞ within the range $n \in \{13, \ldots, 34\}$ and estimated $\rho \approx 13$ from Figure 1 (indicated there by the dotted vertical lines). From Figure 2 one can guess that there are two scatterers, one being located in the lower left vicinity of the origin and the other one in the upper right quarter of the window $[-11, 11]^2$. For ease of completeness we recapitulate that the wave number is $k = 1$, and that the two objects are sound-soft scatterers, whose diameters have about the size of one wavelength. The incident field is a plane wave coming from the left; i.e., u^i is as in (2.2) with $d = (1, 0)$.

4. Moving around. As we have mentioned before, some of the poles of an individual Padé approximant will frequently fail to lie close to any of the inclusions Ω_j. To improve the robustness of this method it would therefore be desirable to compute several Padé approximants and to switch to the counting measure induced by the ensemble of all their poles as a means of visualizing the likelihood that scatterers are located in certain parts of the region of interest.

To this end we shift the origin to any arbitrary point $y \in \mathbb{R}^2$ or, rather, keep the origin and move the source F of (2.7) from $\partial\Omega$ to $\partial\Omega - y$; in other words, we consider the radiating solution u_y of the Helmholtz equation (2.6), with F replaced by the (virtual) source F_y given by

$$\langle\, F_y, v \,\rangle \;=\; \int_{\partial\Omega} v(z - y)\psi(z)\, \mathrm{d}s(z) \;=\; \int_{\partial\Omega - y} v(z)\psi(z + y)\, \mathrm{d}s(z) \,.$$

A straightforward computation reveals that this solution has the far field

$$u_y^\infty(\widehat{x}) \;=\; e^{\mathrm{i}ky\cdot\widehat{x}} u^\infty(\widehat{x}) \,, \qquad \widehat{x} \in S^1 \,, \tag{4.1}$$

which is easily computable from the given data u^∞.

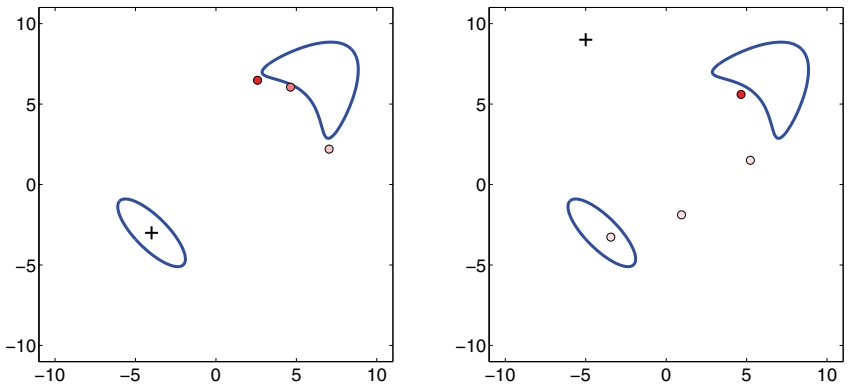

Figure 3. *Localizations of the scatterers for different shifts.*

Note that in general the far field in (4.1) is not the one that would result from a shift of the obstacle from Ω to $\Omega - y$ while the incoming wave is kept fixed. For example, given certain material properties of the scatterers (including the sound-soft and sound-hard cases), it has been exemplified in [28, 31] that the far field corresponding to the shifted obstacle—using the same incoming plane wave u^i of (2.2) with direction d—differs from u_y^∞ of (4.1) by an additional phase shift factor $e^{\mathrm{i}ky\cdot d}$.

The transformation from u^∞ to u_y^∞ has a nontrivial impact on the Fourier spectrum of the far field, which adds additional information to our advantage. We extract this information by running our pole fitting algorithm for several virtual shifts $y \in \mathbb{R}^2$ to gather more (correlated, but seemingly independent) poles to indicate the locations of the scatterers. We expect the results to be best when the different scatterers have similar distance to y, since then the poles of the rational function have comparable size. Figure 3 shows numerical results for the same example as before but now using $y = (-4, -3)$ (resp., $y = (-5, 9)$) as shifts; the respective virtual origins are marked by a + in the plots.

We may conclude from Figures 2 and 3 that some virtual origins may be better suited than others. However, when the virtual origin is moving around in the entire region of interest, and when all poles of the corresponding rational approximations are taken into account, then the corresponding counting measure can, in fact, be used to produce a reasonable visualization of the scatterers (or, rather, their physically relevant features). For an illustration we shift the virtual origin to all 64×64 grid points of an equidistant rectangular grid that covers the region of interest given by the square $[-11, 11]^2$. For each grid point the relevant range of frequencies, i.e., the respective positive indices of the Fourier coefficients of the far field (4.1), is chosen automatically from the data, starting with the second next coefficient to the right of the last local maximum of the absolute values, and ending with the largest frequency, whose coefficient is above 10^{-12} in absolute value. The same procedure is repeated for the Fourier coefficients with negative indices, with straightforward modifications to cope with the differences between (3.7b) and (3.7a). This leads to about 2×10 potential poles per grid point and to a total of more than 32,000 accepted poles within the region of interest. As can be seen from the left-hand plot in Figure 4, those poles cover a large area, and poles can, in fact, be found almost everywhere in a neighborhood of the convex hull of the scatterers.

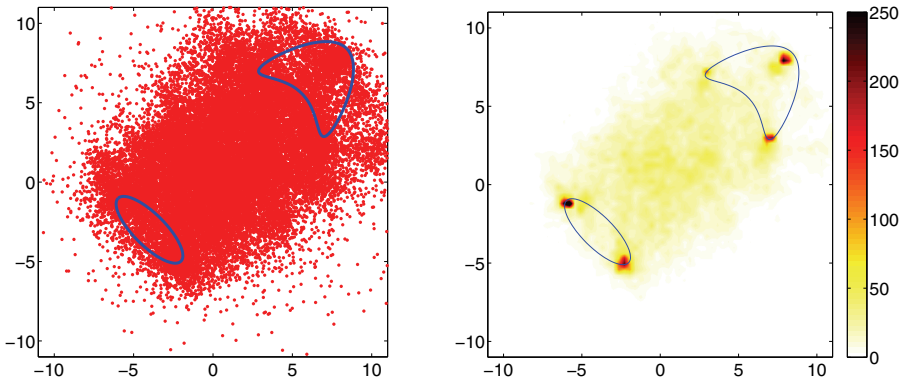

Figure 4. *Localizations of the scatterers for all possible shifts. Left: All poles marked. Right: Counting measure of the poles.*

The color coded right-hand plot in Figure 4, on the other hand, shows the corresponding counting measure, based on the 63×63 cells of our grid. As can be seen, some grid cells do have quite a large pole count this way, whereas most of the grid cells receive only a small number of hits. In fact, the maximum count obtained this way has been 371 for this particular example, which is significantly beyond the cut-off limit of the colorbar (the latter being introduced to enhance more features of the reconstruction). This visualization provides a very good localization of distinct geometrical features of the scatterers, indeed.

5. Tiny inclusions and the effect of noise. As has already been said, the method presented in this paper has the shortcoming that the number of Fourier coefficients that can be used is dramatically reduced in the presence of noise; for the example that we have used for our illustrations so far, the reconstructed images get very bad, even for moderate noise levels.

On the other hand, aiming primarily for approximate source points that match the data, one may hope for better reconstructions if the true scatterers are small compared to the wavelength, say. Our second example therefore consists of a setup with three tiny scatterers: a sound-soft scatterer with the shape of an ellipse centered at $z_1 = (-4, -3)$, a circular scatterer at $z_2 = (4, -8)$ that satisfies an impedance (i.e., Robin) boundary condition, and a sound-hard kite-shaped scatterer positioned at $z_3 \approx (7, 7)$. The diameter of all three scatterers is by a factor of five smaller than in the previous example, whereas the wave number is, again, $k = 1$. This is a typical setting that would call for the MUSIC algorithm if a multistatic scattering matrix were available; see section 6. The present scheme already allows "reconstructions" with one single far field as data, that is, with only one column of this matrix.

In this example we add random Gaussian noise to the 128 far field samples; the relative noise level (i.e., the Euclidean norm of the noise vector divided by the corresponding norm of the exact far field vector) is very moderate, namely 0.001%. We refer to Figure 5 for the Fourier spectrum of the noisy data. As can be seen the noisy plateau of the Fourier coefficients is at a much higher absolute level than in Figure 1, and hence, for the corresponding choice of the origin, only about 2×20 Fourier coefficients can be used for determining approximate source points. In fact, while the total pole count remains similar to the previous example as long as there is no additive noise, the number of accepted poles drops down to only half

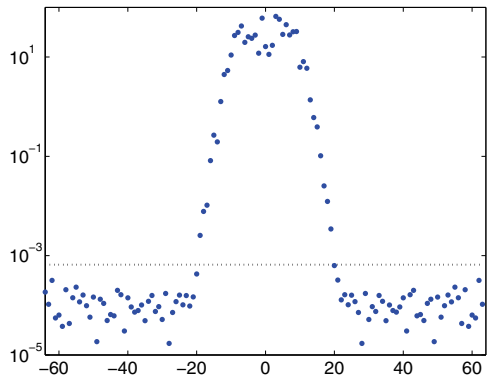

Figure 5. *Noisy Fourier spectrum.*

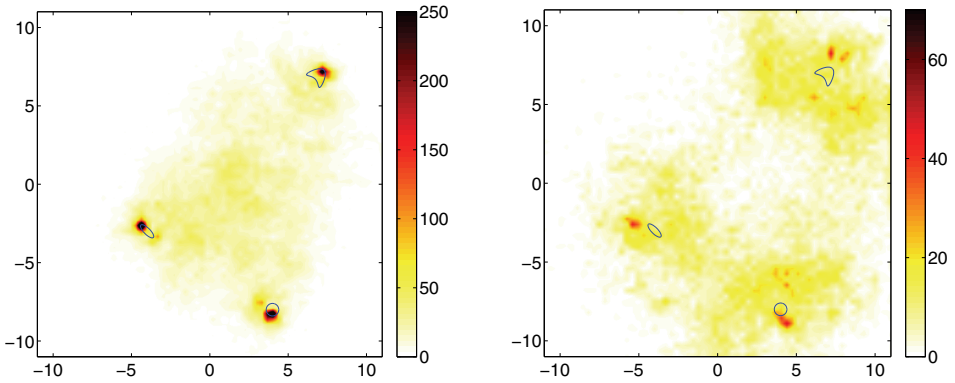

Figure 6. *Reconstruction of the three scatterers with exact data (left) and noisy data (right).*

the previous figure for the noisy data sample. Similarly, the maximal pole count assigned to an individual grid cell is only of the order of 50 as soon as there is noise, rather than a few hundred as before.

The resulting "images" of the three scatterers for exact and noisy data, respectively, are shown in Figure 6. As one can see, while we achieve an excellent image without noise, the reconstruction loses all its focus in the presence of noise: One may still conclude that there are three scatterers, but even this is hard to decide—despite the pretty small amount of noise.

We remark that the reconstructions are qualitatively as good as those obtained in other experiments with data corresponding to true point sources located at the same positions as the three tiny obstacles in Figure 6. This is in agreement with Remark 3.3, that the pole finding algorithm will never be exact, not even for true point sources and infinite accuracy of the given data.

6. A comparison with the MUSIC scheme. The search for small (point) scatterers was the original motivation for this work. As this is the standing assumption of the MUSIC algorithm, a short comparison with this scheme is appropriate.

To begin with, we emphasize the major distinction of our scheme from the MUSIC algorithm: The latter requires *several* columns of the multistatic response matrix for the inversion,

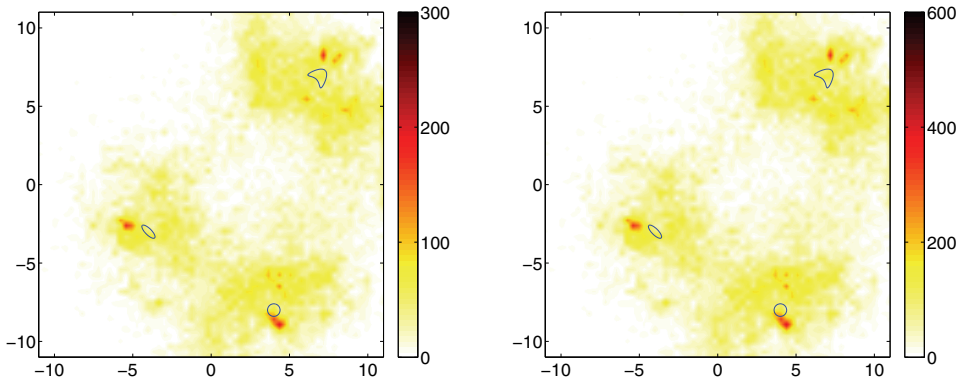

Figure 7. *Reconstruction of three scatterers with noisy data and four (left) and eight (right) incoming waves.*

that is, the far fields corresponding to several incoming waves; to be more precise, if there are J distinct scatterers, then the MUSIC algorithm requires far field data for (at least) J incoming waves. To put this into perspective, there is no similar restriction for our approach: We need only the scattered field for one incident wave.

On the other hand, our scheme has a straightforward extension to the case of multiple far fields, by adding the respective (independent) pole counts for each of the measured fields. It has to be emphasized, though, that each far field will correspond to a different source F in (2.6), each of which is supported on the scatterers, but possibly highlighting different features of them.

Figure 7 shows numerical results for the same setting as in the previous section; in particular, the data share the same amount of noise as before. But now we are using four (resp., eight) incoming plane waves from equidistant directions of S^1. A comparison of the corresponding plots with the right-hand side result in Figure 6 for one incident field reveals only a very minor improvement of the "reconstruction" from multiple pieces of data.

Now we turn to the MUSIC scheme, which has been implemented in the particular version described by Kirsch [25], as this one uses the given far field data. The corresponding reconstructions are shown in Figure 8. It turns out that MUSIC, in general, is the better and more robust imaging technique *provided* that there are sufficiently many incoming waves: For example, when using only four incident fields, the MUSIC scheme fails, as it detects only two of the three scatterers; see the left-hand plot in Figure 8.

In summary, the capability of our scheme to handle a single incident field is its major advantage; MUSIC is not a suitable option for that case. When enough data are available, then the MUSIC scheme is certainly superior. We mention that methods from compressed sensing provide another option for imaging sparse scatterers given only data for one incident field, as has been demonstrated, e.g., in [14].

7. Conclusions. We have shown how to determine—from the far field of a single time-harmonic scattered field—a discrete set of points that provide information about the significant geometrical features of a set of scatterers with unknown physical properties. By repeating this approximation for different points of origin, we have demonstrated how to separate relevant points (i.e., poles) from spurious ones, and how to provide a cartoon of the scatterers, even-

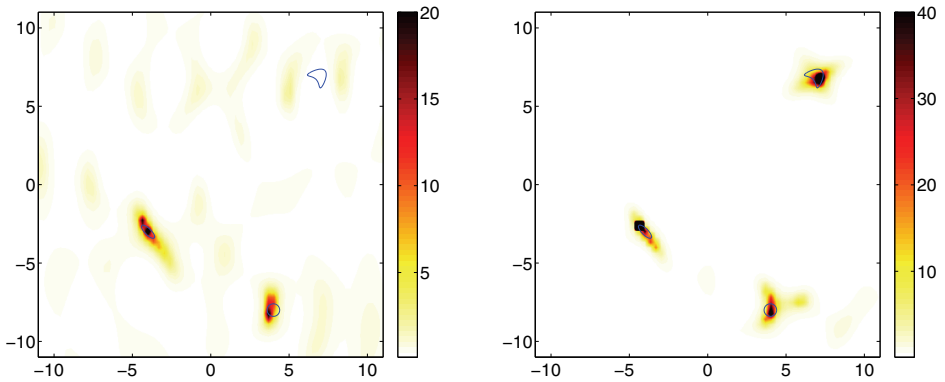

Figure 8. *MUSIC reconstructions of three scatterers with noisy data and four (left) and eight (right) incoming waves.*

tually. Alternatively, given the approximate source points and corresponding residues, one can proceed as in [19] and improve this first estimate of the scatterers with a Newton-type scheme.

The method applies to tiny scatterers, as well as scatterers in the resonance region, and it is extremely fast, as it does not require any forward solves of the scattering problem. On the downside, however, the method is very sensitive to noise. Partly, this is so because the inverse scattering problem with only one piece of data is severely ill-posed. More stable reconstructions might be possible if means were developed to efficiently exploit the low frequencies of the far field's spectrum with its oscillating Fourier coefficients. This is ongoing research.

We finally mention that our approach is not restricted to the particular setting that we have been focusing on. For example, if near field rather than far field data are given, on a circle of radius r, say, that encloses the scatterers, then the Fourier transform of the far field is easily deduced from the Fourier transform of the near field, as the scattered field allows the representation (cf., e.g., [9])

$$u(r\widehat{x}) \;=\; e^{\mathrm{i}\pi/4}\sqrt{\pi k/2}\,\sum_{n=-\infty}^{\infty} \mathrm{i}^n a_n H_n^{(1)}(kr)\, e^{\mathrm{i}nt}$$

for $\widehat{x} = (\cos t, \sin t) \in S^1$, where $H_n^{(1)}$ are the Hankel functions of the first kind of order n, and a_n are the Fourier coefficients of the far field; cf. (2.10).

Also, if the differential equation (2.3) is posed on a bounded domain $D \setminus \overline{\Omega}$ rather than the full space, where $D \subset \mathbb{R}^2$ is a simply connected domain that contains $\overline{\Omega}$, and if Cauchy data of the corresponding solution w are given on the boundary of D, then the problem can be recast as an inverse source problem (2.6) for the full space by defining

$$u(x) \;=\; \int_{\partial D} \left(\Phi(x,z)\,\frac{\partial}{\partial \nu} w(z) \;-\; \frac{\partial \Phi(x,z)}{\partial \nu(z)}\, w(z) \right) \mathrm{d}s(z) \tag{7.1}$$

for $x \in \mathbb{R}^2 \setminus \overline{D}$. In fact, as $\Phi(x, \cdot\,)$ and w are solutions of the homogeneous Helmholtz equation

in $D \setminus \overline{\Omega}$, the potential u of (7.1) can alternatively be represented as

$$u(x) = \int_{\partial\Omega} \left(\Phi(x,z) \frac{\partial}{\partial \nu} w(z) - \frac{\partial \Phi(x,z)}{\partial \nu(z)} w(z) \right) \mathrm{d}s(z) ,$$

which is a radiating solution of the homogeneous Helmholtz equation in $\mathbb{R}^2 \setminus \overline{\Omega}$ and which can be further extended (by zero, say) to a solution of (2.6) for an appropriate distribution F of the form (2.7). Using (2.8) and (A.3), the far field of u is easily determined numerically from (7.1), and hence we are back to the setting of section 2.

Appendix. In (2.5) we have made the assumption that the scattered field u can be represented as a single layer potential over $\partial\Omega$, which is true for sound-soft obstacles or if k is no interior Dirichlet eigenvalue of the Laplacian in Ω; cf., e.g., Potthast, Sylvester, and Kusiak [35, Lemma 3.6].

If some of the scatterers happen to have other material properties, then we can always consider u as the solution of an exterior Dirichlet problem with $g = u|_{\partial\Omega}$ as given Dirichlet data, in which case we can represent u as a combined single and double layer potential

$$u(x) = \int_{\partial\Omega} \Phi(x,z)\psi(z)\,\mathrm{d}s(z) + \mathrm{i} \int_{\partial\Omega} \frac{\partial \Phi(x,z)}{\partial \nu(z)} \psi(z)\,\mathrm{d}s(z) \tag{A.1}$$

for $x \in \mathbb{R}^2 \setminus \overline{\Omega}$, instead of (2.5). The density function ψ can be determined from the jump relations of single and double layer potentials; cf. [9]. In what follows we will investigate only how the presence of the double layer integral

$$u'(x) = \mathrm{i} \int_{\partial\Omega} \frac{\partial \Phi(x,z)}{\partial \nu(z)} \psi(z)\,\mathrm{d}s(z) \tag{A.2}$$

in (A.1) influences the Fourier coefficients of the far field u^∞.

To this end we note that the far field $\Psi_p^\infty(\,\cdot\,,z)$ of

$$\Psi_p(x,z) = p \cdot \operatorname{grad}_z \Phi(x,z) = \frac{\mathrm{i}k}{4} \frac{(x-z)\cdot p}{|x-z|} H_1^{(1)}(k|x-z|) ,$$

where $p \in S^1$, is given by

$$\Psi_p^\infty(\widehat{x},z) = \frac{e^{-\mathrm{i}\pi/4}\sqrt{k}}{\sqrt{8\pi}} (\widehat{x}\cdot p) e^{-\mathrm{i}k\widehat{x}\cdot z} , \qquad \widehat{x} \in S^1 . \tag{A.3}$$

Now inserting the Jacobi–Anger expansion (2.9) we obtain

$$\Psi_p^\infty(\widehat{x},z) = \frac{e^{-\mathrm{i}\pi/4}\sqrt{k}}{\sqrt{8\pi}} (\widehat{x}\cdot p) \sum_{n=-\infty}^{\infty} (-\mathrm{i})^n e^{-\mathrm{i}n \arg z} J_n(k|z|)\, e^{\mathrm{i}nt}$$

for $\widehat{x} = (\cos t, \sin t)$, $0 \le t < 2\pi$. Rewriting

$$\widehat{x}\cdot p = \cos(t-\beta) = \frac{1}{2}\left(e^{-\mathrm{i}\beta} e^{\mathrm{i}t} + e^{\mathrm{i}\beta} e^{-\mathrm{i}t} \right) ,$$

where we have set $\beta = \arg p$, we eventually find the Fourier series

$$\Psi_p^\infty(\widehat{x}, z) \;=\; \frac{e^{-\mathrm{i}\pi/4}\sqrt{k}}{\sqrt{32\pi}} \sum_{n=-\infty}^{\infty} \alpha_n(z,p)\, e^{\mathrm{i}nt}$$

with

$$\alpha_n(z,p) \;=\; (-\mathrm{i})^{n-1} e^{-\mathrm{i}(n-1)\varphi} e^{-\mathrm{i}\beta} \Big(J_{n-1}(k|z|) \;-\; e^{2\mathrm{i}(\beta-\varphi)} J_{n+1}(k|z|) \Big)\,,$$

where $\varphi = \arg z$. Again using the asymptotics (2.12) for the Bessel functions, we deduce that

$$\alpha_n(z,p) \;\approx\; \big(|z| e^{-\mathrm{i}\varphi}\big)^{n-1} e^{-\mathrm{i}\beta}\, \frac{1}{\Gamma(n)} \left(\frac{-\mathrm{i}k}{2} \right)^{n-1}, \qquad n \gg k|z|\,.$$

It thus follows that the double layer potential u' of (A.2) introduces a far field component

$$u'^{\infty}(\cos t, \sin t) \;=\; \sum_{n=-\infty}^{\infty} a'_n e^{\mathrm{i}nt}\,,$$

where (again in complex variable notation)

$$a'_n \;\approx\; \frac{e^{\mathrm{i}\pi/4}\sqrt{k}}{\sqrt{32\pi}}\, \frac{1}{\Gamma(n)} \left(\frac{-\mathrm{i}k\rho}{2} \right)^{n-1} \int_{\partial\Omega} \left(\frac{\overline{\zeta}}{\rho} \right)^{n-1} e^{-\mathrm{i}\beta(\zeta)} \psi(\zeta)\, \mathrm{d}s\,, \qquad n \gg k\rho\,,$$

and $\beta(\zeta)$ denotes the polar angle of the outer normal $\nu(\zeta)$ at $\zeta \in \partial\Omega$.

The same transformation as in (3.6) thus yields

$$c'_n \;=\; \Gamma(n+1) \left(\frac{2}{\mathrm{i}k\rho} \right)^n \frac{\sqrt{8\pi k}}{e^{-\mathrm{i}\pi/4}}\, \overline{a'_n} \;\approx\; n \int_{\partial\Omega} \left(\frac{\zeta}{\rho} \right)^{n-1} \overline{\psi'(\zeta)}\, \mathrm{d}s$$

for $n \gg k\rho$, where

$$\psi'(\zeta) \;=\; \frac{\mathrm{i}}{\rho}\, e^{-\mathrm{i}\beta(\zeta)} \psi(\zeta)\,, \qquad \zeta \in \partial\Omega\,.$$

Assuming, in analogy to (3.3), that

$$\overline{\psi'}\, \mathrm{d}s(\partial\Omega) \;\approx\; \sum_{l=1}^{M} \lambda'_l \delta_{\rho\widehat{\zeta}'_l}$$

for certain points $\widehat{\zeta}'_l$ within the unit disk, and having coefficients $\lambda'_l \in \mathbb{C}$, then we obtain that

$$c'_n \;\approx\; b'_n \;=\; n \sum_{l=1}^{M} \lambda'_l \widehat{\zeta}'^{\,n-1}_l\,, \qquad n \gg k\rho\,,$$

where the right-hand side members are the Fourier coefficients of

$$\sum_{n=1}^{\infty} b'_n \widehat{\zeta}^{-n-1} \;=\; -\frac{\mathrm{d}}{\mathrm{d}\widehat{\zeta}} \sum_{l=1}^{M} \frac{\lambda'_l}{\widehat{\zeta}'_l} \sum_{n=1}^{\infty} \left(\frac{\widehat{\zeta}'_l}{\widehat{\zeta}} \right)^n \;=\; \sum_{l=1}^{M} \frac{\lambda'_l}{(\widehat{\zeta} - \widehat{\zeta}'_l)^2}\,.$$

We conclude that the presence of the double layer potential u' in (A.1) manifests itself via the appearance of double poles of the rational approximations. As a consequence, the combined ansatz (A.1) neither affects the pole finding algorithm, nor its justification to localize scatterers.

Acknowledgments. The author is indebted to Dr. Roland Griesmaier for many inspiring discussions on this topic and for providing the far field data that have been used in this work. The constructive feedback of the referees has also been greatly appreciated.

REFERENCES

[1] G. Alessandrini and L. Rondi, *Determining a sound-soft polyhedral scatterer by a single far-field measurement*, Proc. Amer. Math. Soc., 133 (2005), pp. 1685–1691.
[2] G. Ammar, W. Dayawansa, and C. Martin, *Exponential interpolation: Theory and numerical algorithms*, Appl. Math. Comput., 41 (1991), pp. 189–232.
[3] H. Ammari, *An Introduction to Mathematics of Emerging Biomedical Imaging*, Springer, Berlin, 2008.
[4] H. Ammari, J. Garnier, V. Jugnon, and H. Kang, *Stability and resolution analysis for a topological derivative based imaging functional*, SIAM J. Control Optim., 50 (2012), pp. 48–76.
[5] H. Ammari, E. Iakovleva, and S. Moskow, *Recovery of small inhomogeneities from the scattering amplitude at a fixed frequency*, SIAM J. Math. Anal., 34 (2003), pp. 882–900.
[6] H. Ammari and H. Kang, *Reconstruction of Small Inhomogeneities from Boundary Measurements*, Springer, Berlin, 2004.
[7] G.A. Baker and P. Graves-Morris, *Padé Approximants*, 2nd ed., Cambridge University Press, Cambridge, UK, 1996.
[8] L. Baratchart, J. Leblond, F. Mandréa, and E.B. Saff, *How can the meromorphic approximation help to solve some 2D inverse problems for the Laplacian?*, Inverse Problems, 15 (1999), pp. 79–90.
[9] D. Colton and R. Kress, *Inverse Acoustic and Electromagnetic Scattering Theory*, 2nd ed., Springer, Berlin, 1998.
[10] D. Colton and B.D. Sleeman, *Uniqueness theorems for the inverse problem of acoustic scattering*, IMA J. Appl. Math., 31 (1983), pp. 253–259.
[11] A.J. Devaney, *Super-resolution Processing of Multi-static Data Using Time Reversal and MUSIC*, manuscript, 2000.
[12] A. El Badia and T. Ha-Duong, *An inverse source problem in potential analysis*, Inverse Problems, 16 (2000), pp. 651–663.
[13] J. Elschner and M. Yamamoto, *Uniqueness in determining polygonal sound-hard obstacles with a single incoming wave*, Inverse Problems, 22 (2006), pp. 355–364.
[14] A.C. Fannjiang, T. Strohmer, and P. Yan, *Compressed remote sensing of sparse objects*, SIAM J. Imaging Sci., 3 (2010), pp. 595–618.
[15] G.R. Feijoo, *A new method in inverse scattering based on the topological derivative*, Inverse Problems, 20 (2004), pp. 1819–1840.
[16] I.S. Gradshteyn and I.M. Ryzhik, *Table of Integrals, Series, and Products*, 7th ed., Academic Press, New York, 2007.
[17] R. Griesmaier, *Multi-frequency orthogonality sampling for inverse obstacle scattering problems*, Inverse Problems, 27 (2011), 085005.
[18] M. Hanke, *On real-time algorithms for the location search of discontinuous conductivities with one measurement*, Inverse Problems, 24 (2008), 045005.
[19] M. Hanke and W. Rundell, *On rational approximation methods for inverse source problems*, Inverse Probl. Imaging, 5 (2011), pp. 185–202.
[20] D.J. Hansen and M.S. Vogelius, *High frequency perturbation formulas for the effect of small inhomogeneities*, J. Phys. Conf. Ser., 135 (2008), 012106.
[21] F.B. Hildebrand, *Introduction to Numerical Analysis*, 2nd ed., McGraw–Hill, New York, 1974.
[22] M. Ikehata, *The Herglotz wave function, the Vekua transform and the enclosure method*, Hiroshima Math. J., 35 (2005), pp. 485–506.
[23] W.A. Imbriale and R. Mittra, *The two-dimensional inverse scattering problem*, IEEE Trans. Antennas and Propagation, 18 (1970), pp. 633–642.
[24] T. Johansson and B.D. Sleeman, *Reconstruction of an acoustically sound-soft obstacle from one incident field and the far-field pattern*, IMA J. Appl. Math., 72 (2007), pp. 96–112.

[25] A. Kirsch, *The MUSIC algorithm and the factorization method in inverse scattering theory for inhomogeneous media*, Inverse Problems, 18 (2002), pp. 1025–1040.
[26] A. Kirsch, R. Kress, P. Monk, and A. Zinn, *Two methods for solving the inverse acoustic scattering problem*, Inverse Problems, 4 (1988), pp. 749–770.
[27] R. Kress and W. Rundell, *A quasi-Newton method in inverse obstacle scattering*, Inverse Problems, 10 (1994), pp. 1145–1157.
[28] R. Kress and W. Rundell, *Inverse obstacle scattering with modulus of the far field pattern as data*, in Inverse Problems in Medical Imaging and Nondestructive Testing, H.W. Engl, A.K. Louis, and W. Rundell, eds., Springer, Wien, 1997, pp. 75–92.
[29] S. Kusiak and J. Sylvester, *The scattering support*, Comm. Pure Appl. Math., 56 (2003), pp. 1525–1548.
[30] S. Kusiak and J. Sylvester, *The convex scattering support in a background medium*, SIAM J. Math. Anal., 36 (2005), pp. 1142–1158.
[31] J.J. Liu and J.K. Seo, *On stability for a translated obstacle with impedance boundary condition*, Nonlinear Anal., 59 (2004), pp. 731–744.
[32] D.S. Lubinsky, *Rogers-Ramanujan and the Baker-Gammel-Wills (Padé) conjecture*, Ann. of Math. (2), 157 (2003), pp. 847–889.
[33] R. Potthast, *A point source method for inverse acoustic and electromagnetic obstacle scattering problems*, IMA J. Appl. Math., 61 (1998), pp. 119–140.
[34] R. Potthast, *A study on orthogonality sampling*, Inverse Problems, 26 (2010), 074015.
[35] R. Potthast, J. Sylvester, and S. Kusiak, *A "range test" for determining scatterers with unknown physical properties*, Inverse Problems, 19 (2003), pp. 533–547.
[36] C. W. Therrien, *Discrete Random Signals and Statistical Signal Processing*, Prentice–Hall, Englewood Cliffs, NJ, 1992.